Kent Academic Repository

Full text document (pdf)

Citation for published version

Burchell, M.J. and Morris, A.J.W. (2017) Laboratory tests of catastrophic disruption of rotating bodies. Icarus, 296 . pp. 91-98. ISSN 0019-1035.

DOI

https://doi.org/10.1016/j.icarus.2017.05.016

Link to record in KAR

http://kar.kent.ac.uk/61927/

Document Version

Publisher pdf

Copyright & reuse
Content in the Kent Academic Repository is made available for research purposes. Unless otherwise stated all content is protected by copyright and in the absence of an open licence (eg Creative Commons), permissions for further reuse of content should be sought from the publisher, author or other copyright holder.

Versions of research
The version in the Kent Academic Repository may differ from the final published version.
Users are advised to check **http://kar.kent.ac.uk** for the status of the paper. **Users should always cite the published version of record.**

Enquiries
For any further enquiries regarding the licence status of this document, please contact:
researchsupport@kent.ac.uk

If you believe this document infringes copyright then please contact the KAR admin team with the take-down information provided at **http://kar.kent.ac.uk/contact.html**

KAR Kent Academic Repository

University of Kent

Icarus 296 (2017) 91–98

Contents lists available at ScienceDirect

Icarus

journal homepage: www.elsevier.com/locate/icarus

Laboratory tests of catastrophic disruption of rotating bodies

A.J.W. Morris, M.J. Burchell*

Centre for Astrophysics and Planetary Science, School of Physical Sciences, University of Kent, Canterbury, Kent CT2 7NH, United Kingdom

ARTICLE INFO

Article history:
Received 10 October 2016
Revised 23 March 2017
Accepted 24 May 2017
Available online 26 May 2017

Keywords:
Collisional physics
Cratering
Impact processes
Asteroid
Rotation

ABSTRACT

The results of catastrophic disruption experiments on static and rotating targets are reported. The experiments used cement spheres of diameter 10 cm as the targets. Impacts were by mm sized stainless steel spheres at speeds of between 1 and 7.75 km s^{-1}. Energy densities (Q) in the targets ranged from 7 to 2613 J kg^{-1}. The experiments covered both the cratering and catastrophic disruption regimes. For static, i.e. non-rotating targets the critical energy density for disruption (Q^*, the value of Q when the largest surviving target fragment has a mass equal to one half of the pre-impact target mass) was $Q^* = 1447 \pm 90$ J kg^{-1}. For rotating targets (median rotation frequency of 3.44 Hz) we found $Q^* = 987 \pm 349$ J kg^{-1}, a reduction of 32% in the mean value. This lower value of Q^* for rotating targets was also accompanied by a larger scatter on the data, hence the greater uncertainty. We suggest that in some cases the rotating targets behaved as static targets, i.e. broke up with the same catastrophic disruption threshold, but in other cases the rotation helped the break up causing a lower catastrophic disruption threshold, hence both the lower value of Q^* and the larger scatter on the data. The fragment mass distributions after impact were similar in both the static and rotating target experiments with similar slopes.

© 2017 The Authors. Published by Elsevier Inc.
This is an open access article under the CC BY license. (http://creativecommons.org/licenses/by/4.0/)

1. Introduction

Impacts are a common evolutionary process for solar system bodies (e.g. see Osinski and Pierazzo, 2013 for a recent discussion). For large bodies, the impacts mostly alter the surface, but as bodies become smaller the risk increases of a catastrophic break-up of the target body. The presence of asteroid families in the asteroid belt (see Cellino et al., 2009, for a review), illustrates the outcomes of such break-ups when the energy injected into the system is not only sufficient to break the target apart, but also to disperse the fragments against their own self gravity.

To judge the likely outcome of an impact (cratering or disruption), a parameter is needed which scales with the sizes of the bodies involved. The energy density (Q) is therefore used, defined as the kinetic energy input by the impactor, divided by the total mass of the two bodies (m_p, impactor mass, and M_t, target mass). Since the mass of the target is usually significantly greater than that of impactor, the energy density is often taken as:

$$Q = \frac{m_p v_p^2}{2\, M_t} \tag{1}$$

This Q parameter is used extensively throughout the field of catastrophic disruption research. An alternative formulism for Q exists for planetesimal formation considerations in terms of reduced mass (Stewart and Leinhardt, 2009). This alternative adaptation of the energy density equation was to allow for the level of momentum transfer between the projectile and the target body being impacted, in the case where the projectile was comparable in size to the target. In the work here the impactor will be significantly smaller than the target, so the standard definition of Eq. (1) is used for Q.

The cratering regime of hypervelocity impacts onto targets is taken to apply for values of Q which result in the remaining mass from the target body being greater than 50% of the initial mass. At the 50% point in remnant mass, Q is known as Q^* and represents the start of catastrophic disruption. Strictly speaking there is a complication, as indicated above, concerning re-accumulation under self gravity. For very small bodies this is a negligible effect. But for bodies about 50 or 100 m in size, the extra energy needed to disperse the fragments of the shattered body adds significantly to Q^*. There are thus two target size regimes important in catastrophic disruption e.g. small sizes which are strength dominated (and where Q^* falls as target body size increases) and large sizes which are gravity dominated (where Q^* increases with body size). A review of this behaviour is given in Holsapple et al. (2002). This result is also shown in typical modelling results of catastrophic

* Corresponding author.
E-mail address: M.J.Burchell@kent.ac.uk (M.J. Burchell).

http://dx.doi.org/10.1016/j.icarus.2017.05.016
0019-1035/© 2017 The Authors. Published by Elsevier Inc. This is an open access article under the CC BY license. (http://creativecommons.org/licenses/by/4.0/)

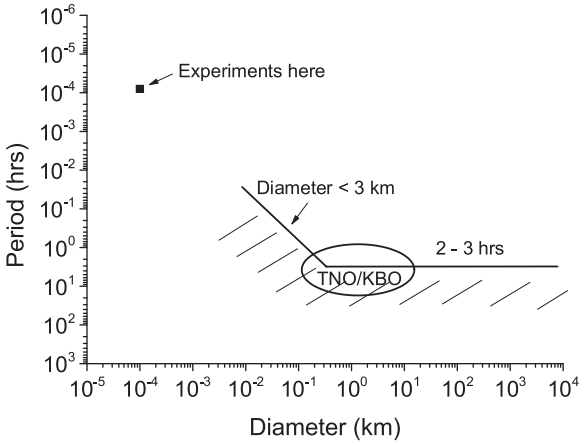

Fig. 1. Spin period vs. diameter for small bodies in the solar system (adapted from Fig. 1 in Holsapple, 2007). For asteroid diameters > 3 km the upper limit on the period is some 2 – 3 h, and for smaller sizes the period decreases. The periods of Trans-Neptunian Objects (TNO) and Kuiper Belt Objects (KBO) are also shown. The objects used in the experiments here (10 cm diameter, period 0.29 s) appear top left and can be seen to lie on the extrapolated trend line for small asteroids.

disruption such as the hydrocode work of Benz and Asphaug (1999) and the recent analytic model of Leliwa-Kopystyński et al. (2016).

However, despite the wealth of experimental and computational work into catastrophic disruption (e.g. Holsapple et al., 2002, and the references therein, and more recent work such as Granvick et al., 2016), one major aspect has remained untested experimentally, namely what if the target is rotating? All previous laboratory experimental work has used static targets. However, real solar system bodies rotate (see Fig. 1). The rotation rates of asteroids for example are well measured and the mechanisms behind asteroid dynamics are now widely studied, e.g. the YORP and Yarkovsky effects (see Bottke et al., 2006 for a review).

The question that arises is whether Q^* varies with rotational rate. Rotation effectively adds a stress into a body, indeed superfast rotators may tear themselves apart. Given that many asteroids are held to be aggregate bodies and not monoliths, this is perhaps not too surprising. Recent modelling of catastrophic disruption of km-sized rotating bodies suggests the pre-impact rotation can play a role in the outcome of the event, reducing Q^* by around 6% (Ballouz et al., 2014,2015). However, earlier modelling of impacts on rotating rubble piles had suggested the pre-impact rotation did not influence Q^* significantly (Takeda and Ohtsuki, 2009).

The ability to refine theoretical and computational models on catastrophic disruption is of great importance, and therefore being able to make models as close to observations is key. It is thus important to undertake laboratory experiments to determine what happens in impacts on rotating objects. This is what is reported here.

2. Method

This work created hypervelocity impacts in the laboratory using a two stage light gas gun. The gun used was at the University of Kent and is described in Burchell et al. (1999). It fires a nylon sabot (discarded in flight) inside which is mounted a projectile which proceeds alone to the target. In this work the projectiles were stainless steel spheres, ranging in size from 1.0 to 2.5 mm diameter. The impact speed was varied from shot to shot (see Burchell et al., 1999, for a discussion of how this is done). In this work, the impact speed ranged from around 1 to 7.75 km s^{-1}, with most shots in the range 4 – 5 km s^{-1}, close to the 5 km s^{-1} estimated as the mean collisional speed in the asteroid belt (Bottke et al., 1994). The

Fig. 2. Cement sphere after manufacture.

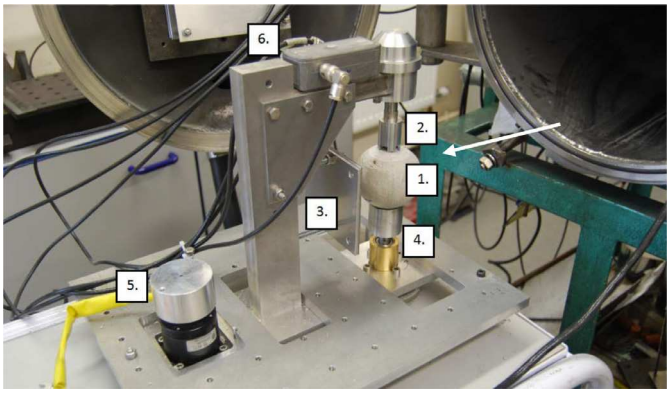

Fig. 3. The rotating target holder (made from aluminium) holding a cement target. Labels indicate: 1 - target, 2 – upper support, 3 – rear shield protect frame from impact ejecta, 4 – lower support, 5 – vacuum motor and 6 – electrical relays.

speed inside each shot was measured to better than ± 1% by the projectile interrupting two laser light stations whilst in flight. Each laser was focussed on a photodiode, and the interruption in signal provided timing information which gave the speed. The target chamber was evacuated to around 0.5 mbar during each shot.

The targets used were cement spheres made in the laboratory. They were typically 10 cm in diameter, with each sphere measured and weighed before use. The typical mass pre-shot was 368 g and was measured to ± 0.1 g. The cement (LaFarge Portland Cement) was mixed with water with a ratio of cement to water of 7:3. This ratio was varied in tests and found to produce the strongest cement samples after curing (in agreement with the work of Brandt, 1998). Care was taken to avoid formation of macroscopic voids during the casting process which poured the cement into spherical moulds. Tests on samples of cement cured in cylindrical moulds gave a compressive strength of 180 MPa and a tensile strength of 1.1 MPa. A typical target sphere is shown in Fig. 2.

To rotate the targets a device was made which held the sphere between two metal rods mounted vertically, spinning about the vertical axis running though the rods and the centre of the target. This is shown in Fig. 3. Since the rotating holder was to operate in the target chamber, a vacuum rated motor and set of electronics had to be used. The impact direction onto the target is shown with an arrow (in Fig. 3). The rotation frequency was set to be 3.44 Hz on average, i.e. a period of 0.29 s. In the experiments reported the median frequency was indeed 3.44 Hz, with a mean of 3.47 ± 0.11 Hz. This was chosen so that, combined with the target size, the experiments would correspond to the position shown on Fig. 1, which extrapolates from the period-sized relationship observed for small asteroids. The position of the targets was aligned

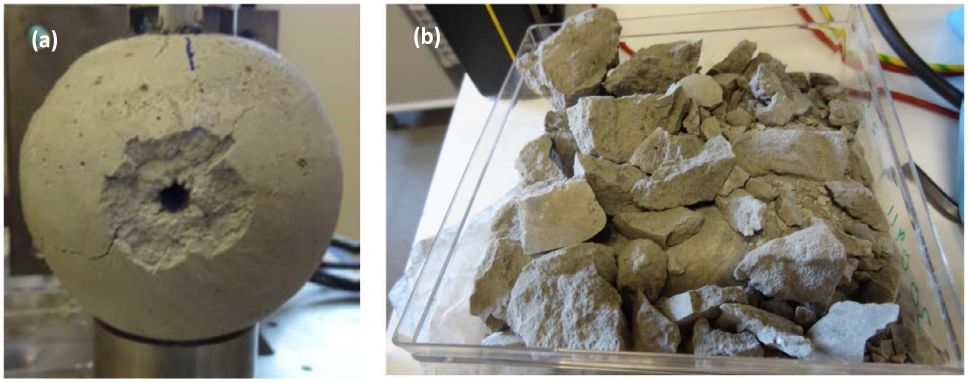

Fig 4. Targets after impact. (a) Cratering event. (b) Catastrophically disrupted target.

Table 1
Shot conditions for static (non-rotating) targets. The ratio m_f/m_o is the mass of the largest fragment (m_f) divided by the pre-impact mass (m_o). Q is the impact energy density.

Projectile dia. (mm)	Impact speed (km s^{-1})	m_f/m_o	Q (J kg^{-1})
1.0	1.124	0.99	7
1.0	3.06	0.99	52
2.0	1.731	0.98	117
1.0	7.5	0.92	280
3.0	1.954	0.97	518
2.0	3.87	0.80	592
2.5	3.05	0.72	701
2.0	4.58	0.72	861
2.0	4.83	0.70	930
2.5	3.75	0.20	1177
2.0	5.68	0.49	1428
2.5	4.28	0.55	1493
2.5	4.57	0.58	1655
2.5	4.44	0.11	1765
2.5	4.69	0.38	1868
3.0	3.81	0.17	2144
3.0	3.79	0.19	2337
3.0	4.36	0.04	2609
3.0	4.25	0.04	2613

with the axis of the gun, such that impacts were equatorial and at normal incidence in line with the centre of mass of the target.

After a shot the outcomes were a cratered target, or a catastrophically disrupted target (see Fig. 4a and b respectively). In the former case the sphere was removed from the target chamber and weighed, and the observed crater measured. If the target was disrupted, the fragments were collected and weighed. It is possible that the fragments impacted the mounting frame and underwent further damage, however this effect is held to be minimal.

3. Disruption limit for static, i.e. non-rotating targets

To establish a baseline set of measurements, a series of 19 shots were done on non-rotating targets. To achieve this, the targets were still mounted in the rotating target holder, but the motor was not turned on. By varying the projectile size and speed, the impact energy density Q was varied from 7 to 2613 J kg^{-1} (see Table 1). Plotting the ratio m_f/m_o (the mass of the largest fragment m_f divided by the original mass m_o) vs. Q, the classic transition from cratering to disruption is seen (Fig. 5a). There is not a smooth transition from cratering to disruption, and some scatter on the data is apparent in Fig. 5a. The uncertainties on the values of m_f/m_o arise from uncertainty in the mass measurement, but the mass balance used was accurate to 0.1 g, and even in the worst case the mass of the largest fragment was around 15 g, giving an uncertainty of less than 1%. Given that the impact speed was also measured to

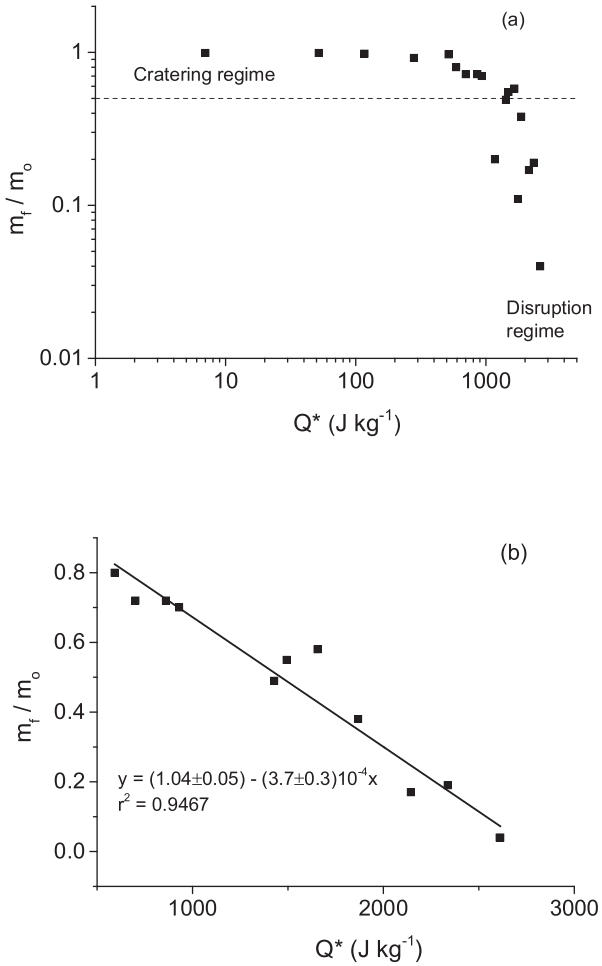

Fig. 5. Surviving mass fraction for largest fragment (m_f/m_o) vs. Q^* for static (i.e. non-rotating targets). (a) All data, showing both cratering and disruption regimes. (b) Events with $Q > 500$ J kg^{-1}, and shows a linear fit to the data.

better than 1%, the scatter on the observed data in Fig. 5a does not arise from measurement errors. There is thus no obvious reason why the shots with Q of 1177 and 1765 J kg^{-1}, gave what appear to be anomalously low values for m_f/m_o. It may be that there were some unrecognised pre-existing flaws in the moulded spheres which lowered the target strength.

Although we cannot explain these anomalous values we exclude them from the calculation of Q^*. Whilst normally this would not be best practice, here these data are significantly off to one side in the data distribution and bias the result accordingly. To find Q^* we also

Table 2
Shot conditions for rotating targets. The ratio m_f/m_o is the mass of the largest fragment (m_f) divided by the pre-impact mass (m_o). Q is the impact energy density. n.r. indicates a shot where the rotation speed was not recorded.

Projectile dia. (mm)	Impact speed (km s^{-1})	Rotation frequency (Hz)	m_f/m_o	Q (J kg^{-1})
1.0	1.19	3.59	0.99	8
1.0	3.07	2.62	0.99	47
2.0	1.63	3.38	0.99	98
3.0	1.00	3.44	0.96	157
1.0	7.75	3.47	0.94	317
3.0	1.93	3.43	0.44	555
2.0	4.05	3.39	0.73	700
2.0	4.00	3.44	0.68	734
2.0	4.71	3.45	0.34	815
2.5	3.46	n.r	0.76	1004
2.5	4.54	3.44	0.32	1061
3.0	2.93	3.44	0.50	1323
2.0	3.86	3.44	0.71	1392
3.0	2.68	3.43	0.14	1388
2.5	3.85	3.43	0.41	1470
2.0	5.78	3.45	0.41	1479
2.5	4.24	3.51	0.79	1493
2.5	4.16	3.43	0.17	1589
2.5	4.09	3.45	0.47	1666
2.0	4.62	3.95	0.21	1784
2.5	4.61	3.45	0.39	2085
3.0	3.62	3.45	0.14	2114
3.0	3.81	3.46	0.13	2326
3.0	4.16	3.46	0.11	2527
3.0	4.07	3.44	0.08	2538

exclude those data which are well within the cratering regime, i.e. $Q < 500$ J kg^{-1} and plot the remaining data on a linear set of axes in Fig. 5b. We then make a linear fit to m_f/m_o vs. Q and obtain the result shown on Fig 5b, namely:

$$m_f/m_o = (1.04 \pm 0.05) - (3.7 \pm 0.3)10^{-4}Q, \; r^2 = 0.9467, \qquad (2)$$

where Q was in J kg^{-1} and r^2 is the square of the regression coefficient.

Given the result in Eq. (2) we can solve for $m_f/m_o = 0.5$, and obtain $Q^* = 1462 \pm 89$ J kg^{-1}. The uncertainty in Q^* comes from the 95% confidence limits after the minimization in the χ^2 value in the linear fit routine used.

4. Disruption limit for rotating targets

A similar procedure to that for the static targets was followed and 25 shots made. Now however, the rotating target holder was powered. The rotation frequency was measured in real time during each shot and is given in Table 2. The data for m_f/m_o vs. Q are plotted in Fig. 6a. Again we can see a cratering regime at low Q values, transiting to the disruption regime at higher Q values.

Looking at Fig 6a, it is clear there is a much larger scatter on the data than before. We considered if this was linked to slight variations in the rotation frequency or mass of the targets, but no pattern emerged. It therefore appears that this is a characteristic of the presence of rotation. As before, to find Q^* we looked at the data points approaching the disruption threshold and beyond (Fig. 6b, corresponding to $Q > 500$ J kg^{-1}), and made a linear fit. We obtained:

$$m_f/m_o = (0.78 \pm 0.11) - (2.56 \pm 0.72)10^{-4}Q, \; r^2 = 0.3782. \qquad (3)$$

The large scatter on the data is reflected in the low r^2 value and the relatively large uncertainty on the value of the slope. We solve for $m_f/m_o = 0.5$, and obtain $Q^* = 1094 \pm 330$ J kg^{-1}. The uncertainty is again given by the 95% confidence bands in the regression fit.

5. Mass distribution of fragments after impact

In each shot the mass of the individual fragments post-shot was found and normalised to the pre-impact target mass. The sensitiv-

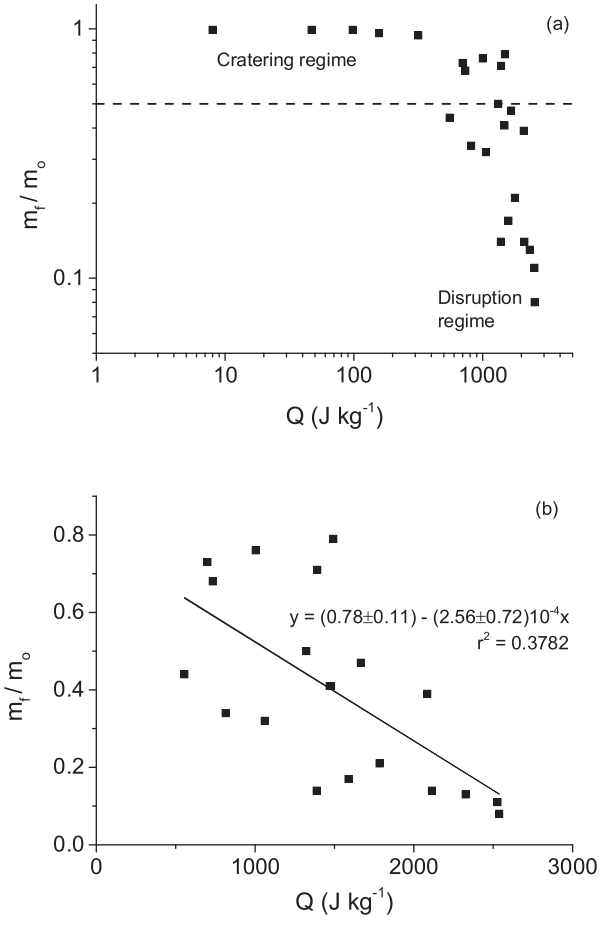

Fig. 6. Surviving mass fraction for largest fragment (m_f/m_o) vs. Q^* for rotating targets. (a) All data (i.e. cratering and disruption regimes). (b) Events with $Q > 500$ J kg^{-1}, and shows a linear fit to the data.

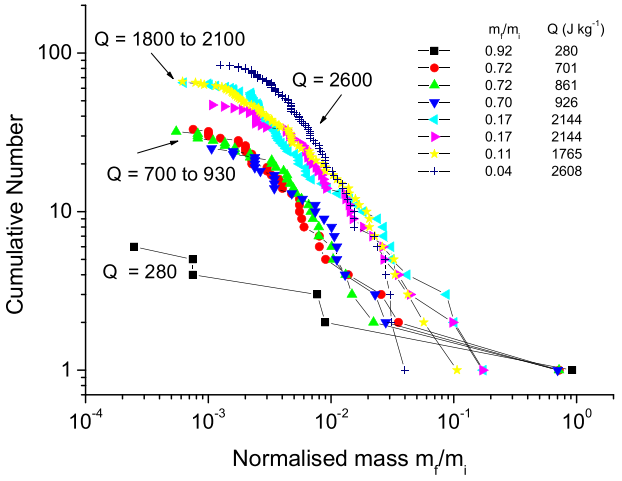

Fig. 7. Cumulative number of fragments with mass greater than m_f/m_o. for impacts on static (i.e. non-rotating) targets.

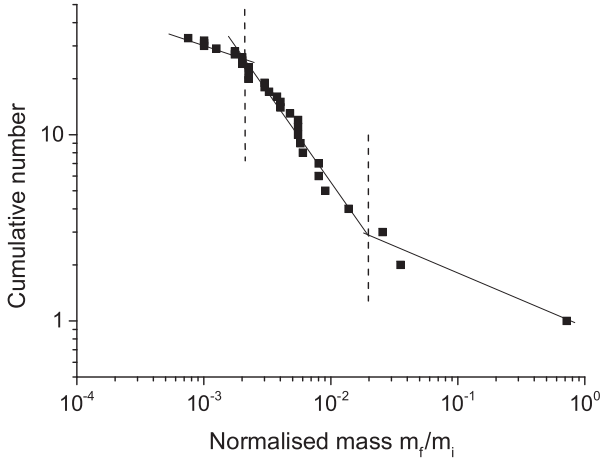

Fig. 8. Cumulative number of fragments with mass greater than m_f/m_o. for impact on a static target at $Q = 701\ J\ kg^{-1}$. The data are split into 3 regions by vertical dashed lines, and the solid lines are indicative fits to the data in each region.

ity of the mass balance used was 0.1 g. Given a typical pre-shot target mass of 360 g, this is equivalent to a minimum measured fractional mass of a fragment of about 5×10^{-4}. Thus the measured fragment masses span over 3 orders of magnitude.

5.1. Static targets

The data for the static target impacts are shown in Fig. 7, where the cumulative number greater than a given normalised mass is plotted vs. normalised mass. We show data for 8 impacts from Table 1 in Fig 7 over a range of Q values. At similar Q values, the data from different impacts group together, indicating reproducibility of the data. There is a clear evolution with increasing Q of the data in Fig. 7, with a general steepening of the slope of the cumulative distribution at higher Q, along with a reduction in size of the largest fragment. In addition another feature is evident in Fig. 7. As events go from $Q < Q^*$ to $Q > Q^*$ the general shape of the cumulative normalised mass distribution for the larger masses, undergoes an evolution: it is concave for sub-critical impacts and convex for disrupted bodies. This has been seen before. For example it was suggested by Tanga et al. (1999) and Durda et al. (2007), that the size frequency distribution could be used to determine if the fragments noted in asteroid families were from sub-critical, or critical, disruption events. Similarly, Leliwa-Kopystynski et al. (2009), argued (by measuring the size distribution functions) that the Eunomia asteroid family arose from a sub-critical impact, whilst the Themis family arose from a disruptive impact on a parent body.

When attempting to fit the data in Fig. 7, it was apparent that a single function did not provide a good description. This is illustrated in Fig. 8 where we show just one event, with $Q = 701\ J\ kg^{-1}$. In this, as in most events, the data seem to fall into three regions of normalised mass $m = m_f/m_o$ (mass fragment / initial target mass) of low mass, intermediate mass and high mass. This has been seen before, e.g. see Fujiwara et al. (1989) or Ryan (2000), for a review. We generally found that we could define the three regions as $m < 0.002$, $0.002 < m < 0.02$ and $m > 0.02$. We fit each region separately with a power law of the form $N = \alpha \times m^{-\beta}$, where N is the cumulative number greater than the given normalised mass m (see for example Fujiwara et al., 1989, for a discussion of the various parametrisations used to describe the fragment mass distributions and the relationships between the various resultant coefficients such as β).

Note that for events with very low Q values, i.e. where a crater was formed in the target, the data do not show this tripartite nature, but can be fit by a single power law. We also note that the roll off in the data at the smallest masses may reflect issues with collecting the finer fragments from the disrupted targets (and we do find very fine fragments after impact which are hard to collect and measure). When considering the results of the fits we therefore do not attach great significance to the β values for $m < 0.002$, other than noting that they typically measure 0.2 – 0.3. For the largest masses ($m > 0.02$), the β values range from typically 0.1 to 0.3 at low Q values (sub-critical impacts) to 1 – 2 at high Q (disruption) and are telling us about the distribution of just the largest few fragments after impact. What happens is that the gap in size between the largest and next largest fragment reduces significantly as we go from sub-catastrophic to catastrophic disruption. This leaves the intermediate size regime where most of the data lay in an event, and we show the value of β vs. Q for all static target impacts events in this normalised fragment mass range in Fig. 9a.

In Fig. 9a, it can be seen that at low Q values, β is around 0.2 – 0.3, rising to around 0.9 for $Q = Q^*$. The value of β does not vary as Q then increases further. If we average the β values for $Q > 1000\ J\ kg^{-1}$, we find $\beta = 0.93 \pm 0.28$, where the error range is 1 standard deviation.

5.2. Rotating targets

As before, we also looked at the fragment size distribution in each shot (Fig. 10). There is a general evolution in fragment size distributions dependent on the degree of disruption. There is the same general shape to the distributions as for the static cases. We split each data set into the three mass ranges as before, and show β for the intermediate size regime in Fig. 9b. We find the same general behaviour as before, i.e. β is low at low Q, rising to a constant value (here around 0.8) for $Q > Q^*$. If we average the β values for $Q > 1000\ J\ kg^{-1}$ we find $\beta = 0.78 \pm 0.20$.

6. Discussion

The value $Q^* = 1447 \pm 90\ J\ kg^{-1}$ for static targets is in the range expected for a "rocky" body of that size at these impact speeds. First principal models exist for predictions of catastrophic disruption, and for example, Leliwa-Kopystynski et al. (2016) predict that for rocky targets of 10 cm diameter, Q^* should lie in the range 400 – 1200 J kg^{-1} (based on the various assumptions made in the model about material strength etc.). Similarly, a range of other authors, using work based on hydrocodes and experiments, predict Q^* for rocky bodies of this size ranging from approximately 500 to

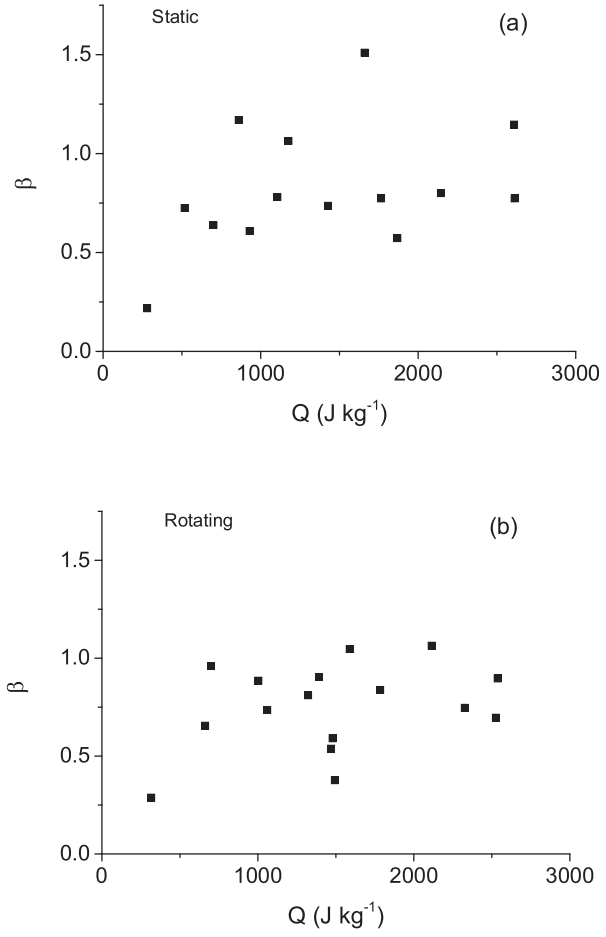

Fig. 9. Slope (β) of power law fits $N = \alpha \times m^{-\beta}$ for the cumulative fragment number distributions. (a) is for static targets, (b) is for rotating targets.

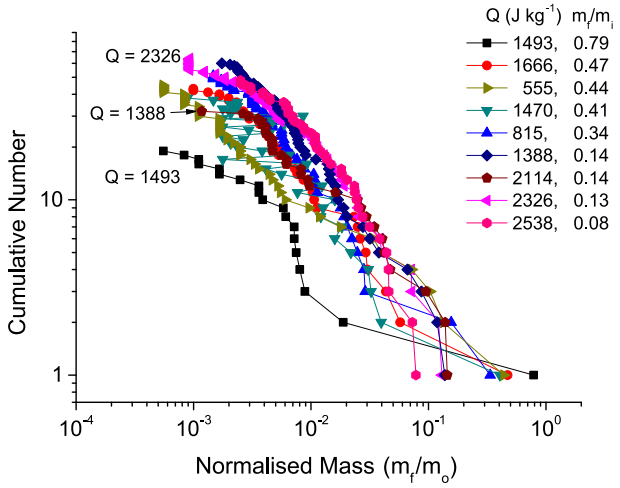

Fig. 10. Cumulative number of fragments with mass greater than m_f/m_o. for impacts on rotating targets.

2000 J kg^{-1} (e.g. Gault and Wedekind, 1969, Housen and Holsapple, 1990; Holsapple, 1994; Durda et al., 1998; Benz and Asphaug, 1999). Indeed Durda et al. (1998), predict a Q^* value for rocky bodies of 8 cm diameter of ~1500 J kg^{-1}.

When comparing the static and rotating cases the most obvious effect is that there is a much greater scatter on the data in the rotating case. There is also a downward shift in Q^* from 1447 ± 90 J kg^{-1} to 987 ± 349 J kg^{-1}. It should be noted however, that whilst the mean value itself has decreased by 32%, the uncertainty has grown.

We suggest the following scenario may apply. At low Q values, well within the cratering regime, the only effect of rotation (if any) may be to remove a bit more spall from around the crater. This has, at best, a modest effect on the removed mass and so has little, if any, influence on m_f/m_o vs. Q in that regime. Effectively, the stress due to rotation, combined with that from the shock from the impact, is still insufficient to lead to breakup of the target. And at very high Q values, well within the disruption regimes, the energy density is such that the stresses from rotation have a minimal contribution compared to the much larger stresses from the passage of the shock waves through the target.

It is thus only in the region around Q^* itself that an effect shows up in the data. The reason being that the extra stress in the target from the impact shock is by itself not quite sufficient to cause the target to break apart. The rotation may however aid the propagation of cracks caused by the impact event, and open them still further, bringing break up at a lower than expected Q value and hence a lowering of Q^* (in this case by approximately 1/3rd). However, this effect on Q^* is only a partial, and not a dominant, effect. Indeed, in some cases it is not quite enough to cause an additional stress which leads to break up, and the target then behaves as in the limiting, static case. This causes the scatter in the data in Fig 6 with a few events behaving as if non-rotating, and others exhibiting a reduction in Q^* due to the rotation. This may be the result of slight in-homogeneities in the target. However, the results suggest that it is the shock from the impact which mostly determines Q^*, and that, at these rotation speeds, the stresses from the rotation are a minor contributor to the overall outcome.

What is not considered here regarding the disruption of rotating targets, is any extra velocity component added to the ejecta. Recently, Strange-Love and Ryan (2015) have looked at this for experimental disruption of static rocky bodies. They found that there is a velocity component both in terms of translational and rotational speed of ejecta fragments (with the further possibility of tumbling). It would be interesting to repeat this for rotating bodies to see how this changes ejecta behaviour. The significance of this may be two fold. First if the translational velocity is altered, dispersion of fragments against self gravity may alter how much material re-accumulates in a subsequent rubble pile. Secondly, the rotation speeds of asteroids which originate from disruption of larger parents which were themselves rotating may also be influenced.

The fragment size distributions show no major change from the static to the rotating targets. For static targets, Gault and Wedekind (1969), reported on fragment size from disruptive impacts on tektites. They found a single power fit the whole size range. However, Takagi et al. (1984), Fujiwara et al. (1989), Davis and Ryan (1990), and Ryan (2000), found that at least two and sometimes three slopes were needed to properly fit fragmentation size distributions as here. Data shown in Fig. 3 of Fujiwara et al. (1989) suggest that for basalt, β is around 0.80 – 0.87. The recent results of Durda et al. (2015) for impacts on basalt spheres, yielded β values in the range 0.75 – 1.2. Both these results are compatible with what is seen here. Durda et al. (2015) reported that the β value increased with increasing Q, but provided no data on this. There is a slight suggestion of this in the data of Fujiwara et al. (1989), but the effect is small, even when Q was varied over 2 orders of magnitude. However, more recently, Michikami et al. (2016), has shown that for impacts on basalt, β varied from 0.4 to 1.1, as Q increased from 150 to 8540 J kg^{-1}. This is very similar to what is found here.

There have also been discussions of fragment shape in various previous publications (see Fujiwara et al., 1989, and Holsapple et al., 2002, for reviews or Durda et al., 2015 and

Michikami et al., 2016 for recent discussions). Here we do not report on this other than to observe that there was no gross difference in the fragment shapes between impacts on static and rotating targets at equal Q. We did however publish a report on fragment shapes inside a similar impact to those reported here in Morris et al. (2013). There we observed that the fragment from the floor of the initial crater formed during the impact, appeared to have similarities in shape to asteroid (2867) Steins.

7. Conclusions

The comparison of impact disruption experiments in static and rotating targets has found a difference in the Q^* value for the small cement targets used. The mean reduction in Q^* of around 32% was also accompanied by increased scatter in the experimental results. This reduction in Q^* could be studied further by significantly increasing or decreasing the rotation frequency, but it should be noted that the present work alone involved 44 separate impact experiments. Also, the experiments here were all for normal incidence, equatorial impacts. Although not investigated here, non-normal incidence on static targets is general considered to decrease cratering efficiency and hence increase Q^*, due to less efficient coupling of the impactor into the target (e.g. see Benz and Asphaug, 1999). The role of polar vs. equatorial impacts cannot be considered in the current experiments due to the nature of the experimental set-up. No difference was observed in the fragment size distributions from the various impacts which were compatible with results of previous work on rocky (basalt) targets.

We note that recent strength tests on cm sized samples of the Tamdakht meteorite, considered to be composed of material similar to Near Earth Asteroids (Binzel et al., 1996), found compressive strengths in the range 26 to 186 MPa (Cotto-Figueroa et al., 2016). Our samples here had a compressive strength of 180 MPa, within the range reported for Tamdakht. However, when considering the extrapolation of these results to larger sizes, i.e., asteroids, it should be noted that it is widely believed that many asteroids are gravitationally bound rubble piles, unlike the targets used here which were intact.

As stated earlier, recent modelling for asteroid disruption carried out by Ballouz et al. (2014),(2015), suggested a 6% reduction in Q^* due to rotation, whilst earlier modelling by Takeda and Ohtsuki (2009) suggested that Q^* for rubble pile asteroids is not greatly influenced by the rotation rate of the target body. The 32% reduction observed here is clearly much larger than expected from the modelling. However, in modelling Q^* is also sensitive to other parameters such as the pore space volume between the components in a rubble pile which increases Q^* (see Deller et al., 2016 for a recent treatment of this). Compaction of pore space requires energy increasing heating effects in the target (see Wünneman et al., 2008). Similarly, laboratory experiments of impacts on porous bodies show that Q^* increases due to porosity (Love et al., 1993; Okamoto et al., 2015) and has to be allowed for along with target strength when parameterising Q^*. Here, we have shown that at laboratory scales, target rotation has an equally significant role in determining Q^*, albeit in an opposite sense (i.e. it lowers rather than raises it).

It would be useful if modellers (either hydrocode or analytical) could adjust their work to include rotation effects on monolithic targets at cm scale to see if they can reproduce this effect. If they can, the work can then be extrapolated to larger scales. In general Q^* falls as object size increases in the strength regime, and then rises with size as gravity starts to dominate. There is thus a minimum in Q^* at some intermediate size, often estimated to be in the range of 1 – 10 km radius for a rocky body. In the absence of such a proper scaling relationship for our results, we can naively imagine that the effect observed here applies equally to the strength part of catastrophic disruption at all size scales. This would lower the Q^* value in the strength regime but leave the gravity dominated regime unchanged. The effect would be to move the minimum in overall Q^* with size, to a smaller size by a factor of around two. Smaller objects than 0.5 – 5 m, would then be easier to disrupt as they will be strength dominated, but larger bodies would be unaffected as Q^* in this case will still be dominated by dispersal against gravity.

Acknowledgments

We thank the Science Technology Facilities Council (UK) for funding of the Kent light gas gun and for a PhD studentship for A. Morris. We thank M. Cole for operation of the light gas gun.

References

Ballouz, R.L., Richardson, D., Michel, P., Schwartz, S., Yu, Y., 2014. Rotation-dependent catastrophic disruption of gravitational aggregates. *Astrophys. J.* 789, 158–169.
Ballouz, R.L., Richardson, D.C., Michel, P., Schwartz, S.R., Yu, Y., 2015. Numerical simulations of collisional disruption of rotating gravitational aggregates: dependence on material properties. Planet. Space Sci. 107, 29–35.
Benz, W., Asphaug, E., 1999. Catastrophic disruption revisited. Icarus 142, 5–20.
Binzel, R.P., Bus, S.J., Burbine, T.H., Sunshine, J.M., 1996. Spectral properties of near-Earth asteroids: evidence for sources of ordinary chondrite meteorites. Science 273, 946–948.
Bottke, W.F., Nolan, M.C., Greenberg, R., Kolvoord, R.A., 1994. Velocity distributions among colliding asteroids. Icarus 107, 255–268.
Bottke Jr., W.F., Vokrouhlicky, D., Rubincam, D.P., Nesvorný, D., 2006. The Yarkovsky and YORP Effects: implications for Asteroid Dynamics. Ann. Rev. Earth Planet. Sci. 34, 157–191.
Brandt, A.M., 1998. Optimisation Methods for Material Design of Cement-Based Composites. Pub. CRC Press, p. 120. Rev. English Ed edition. 328 pages, ISBN-13: 978-0419217909.
Burchell, M.J., Cole, M.J., McDonnell, J.A.M., Zarnecki, J.C., 1999. Hypervelocity impact studies using the 2 MV Van de Graaff dust accelerator and two stage light gas gun of the University of Kent at Canterbury. Meas. Sci. Tech. 10, 41–50.
Cellino, A., Dell'Oro, A., Tedesco, E.F., 2009. Asteroid families: current situation. Planet. Space Sci. 57, 173–182.
Cotto-Figueroa, D., Asphaug, E., Garvie, L.A.J., Rai, A., Johnston, J., Borkowski, L., Datta, S., Chattopadhyay, A., Morris, M.A., 2016. Scale-dependent measurements of meteorite strength: implications for asteroid fragmentation. Icarus 277, 73–77.
Davis, D.R., Ryan, E.V., 1990. On collisional disruption: experimental results and scaling laws. Icarus 83, 156–182.
Deller, J.F., Lowry, S.C., Snodgrass, C., Price, M.C., Sierks, H., 2016. A new approach to modelling impacts on rubble pile asteroid simulants. Mon. Not. R. Astron. Soc. 455, 3752–3762.
Durda, D.A., Greenberg, R., Jedicke, R., 1998. Collisional models and scaling laws: a new interpretation of the shape of the main-belt asteroid size distribution. Icarus 135, 431–440.
Durda, D.D., Bottke Jr., W.F., Nesvorný, D., Enke, B.L., Merline, W.J., Asphaug, E., Richardson, D.C., 2007. Size–frequency distributions of fragments from SPH/*N*-body simulations of asteroid impacts: comparison with observed asteroid families. Icarus 186, 498–516.
Durda, D.D., Campo Bagatin, A., Alemañ, R.A, Flynn, G.J., Strait, M.M., Clayton, A.N., Patmore, E.B., 2015. The shapes of fragments from catastrophic disruption events: effects of target shape and impact speed. Planet. Space Sci. 107, 77–83.
Fujiwara, A., Cerroni, P., Davis, D., Ryan, E., DiMartino, M., Holsapple, K., Housen, K., 1989. Experiments and scaling laws for catastrophic collisions. In: Binzel, R.P., Gehrels, M.S., Matthews, M.S. (Eds.), Asteroids II. University of Arizona Press, Tucson, pp. 240–265.
Gault, D.E., Wedekind, J.A., 1969. The destruction of tektites by meteoroid impact. J. Geophys. Res. 74, 6780–6794.
Granvik, M., Morbidelli, A., Jedicke, R., Bolin, B., Bottke, W.F., Beshore, E., Vokrouhlicky, D., Delbo, M., Michel, P., 2016. Super-catastrophic disruption of asteroids at small perihelion distances. Nature 530 (7590), 303–306.
Holsapple, K.A., 1994. Catastrophic disruptions and cratering of Solar System bodies: a review and new results. Planet. Space Sci. 42, 1067–1078.
Holsapple, K., 2007. Spin limits of Solar System bodies: from the small fast-rotators to 2003EL61. Icarus 187, 500–509.
Holsapple, K., Giblin, I., Housen, K., Nakamura, A., Ryan, E., 2002. Asteroid impacts: laboratory experiments and scaling laws. In: Bottke, Jr., W.F., Cellino, A., Paolichi, P., Binzel, R.P. (Eds.), Asteroids III. Univ. Arizona Press, pp. 443–462. 785 pp.. ISBN 978-0-8165-2281-1.
Housen, K.R., Holsapple, K.A., 1990. On the fragmentation of asteroids and planetary satellites. Icarus 84, 226–253.
Leliwa-Kopystynski, J., Burchell, M.J., Włodarczyk, I., 2009. The impact origin of Eunomia and Themis families. Meteorit. Planet. Sci. 44 (12), 1929–1936.
Leliwa-Kopystyński, J., Włodarczyk, I., Burchell, M.J., 2016. Analytical model of impact disruption of satellites and asteroids. Icarus 268, 266–280.

Love, S.G., Hörz, F., Brownlee, D.E., 1993. Target porosity effects in impact cratering and collisional disruption. Icarus 105, 216–224.
Michikami, T., Hagermann, A., Kadokawa, T., Yoshida, A., Shimada, A., Hasegawa, S., Tsuchiyama, A., 2016. Fragment shapes in impact experiments ranging from cratering to catastrophic disruption. Icarus 264, 316–330.
Morris, A.J.W, Price, M.C., Burchell, M.J., 2013. Is the large crater on asteroid (2867) Steins really an impact crater? Astrophys. J. Lett. 774 (L11), 5. doi:10.1088/2041-8205/774/1/L11.
Okamoto, T., Nakamura, A.M., Hasegawa, S., 2015. Impact experiments on highly porous targets: cavity morphology and disruption thresholds in the strength regime. Planet. Space Sci. 107, 36–44.
Osinski, G.R., Pierazzo, E., 2013. Impact Cratering Processes and Products. Pub. Wiley-Blackwell, West Sussex, UK, p. 316. ISBN 978-1-4051-9829-5.
Ryan, E.V., 2000. Asteroid fragmentation and evolution of asteroids. Annu. Rev. Earth Planet. Sci. 28, 367–389.
Stewart, S.T., Leinhardt, Z.M., 2009. Velocity-dependant catastrophic disruption criteria for planetesimals. Astrophys. J. 691, L133–L137.
Stange-Love, H., Ryan, E.V., 2015. Laboratory impact experiments to study asteroid collisional disruption as a function of size and shape in the strength regime. Procedia Eng. 103, 530–537.
Takeda, T., Ohtsuki, K., 2009. Mass dispersal and angular momentum transfer during collisions between rubble-pile asteroids. II. Effects of initial rotation and spin–down through disruptive collisions. Icarus 202, 514–524.
Takagi, Y., Mizutani, H., Kawakami, S., 1984. Impact fragmentation experiments of basalts and pyrophyllites. Icarus 59, 462–477.
Tanga, P., Cellino, A., Michel, P., Zappalà, V., Paolicchi, P., Dell'Oro, A., 1999. On the size distribution of asteroid families: the role of geometry. Icarus 141, 65–78.
Wünnemann, K., Collins, G.S., Osinski, G.R., 2008. Numerical modelling of impact melt production in porous rocks. Earth Planet. Sci. Lett. 269, 530–539.